Coherent neuronal dynamics driven by optogenetic stimulation in the primate brain

Ryan A. Shewcraft[1], Heather L. Dean[1], Maureen A. Hagan[2,3], Margaret M. Fabiszak[4], Yan T. Wong[2,5,6], and Bijan Pesaran[1,7,8,*]

Lead Contact:
Bijan Pesaran, Ph.D.
4 Washington Pl. Rm 809
Center for Neural Science
New York University
New York, NY 10003 USA
Tel: 212.998.3578, Fax 212.995.4011
E-mail: bijan@nyu.edu

Word counts

Summary	149	(<150)
Introduction	747	
Results	2626	
Discussion	1584	
Methods	2114	
References	62	
Figures	7	
Tables	0	
Total words	4957 (< 5000)	

[1] Center for Neural Science; New York University; New York, NY, 10003; United States
[2] Biomedicine Discovery Institute; Monash University; Clayton, VIC 3800; Australia
[3] Australian Research Council, Centre of Excellence for Integrative Brain Function; Monash University; Clayton, VIC 3800; Australia
[4] Laboratory of Neural Systems; The Rockefeller University; New York, NY, 10065; United States
[5] Department of Electrical and Computer Systems Engineering; Monash University; Clayton, VIC 3800; Australia
[6] Department of Physiology; Monash University; Clayton, VIC 3800; Australia
[7] NYU Neuroscience Institute; New York University Langone Health; New York, NY, 10016; United States
[8] Lead Contact
[*] Correspondence: Bijan@nyu.edu

Summary

Coherent neuronal dynamics play an important role in complex cognitive functions, but the causal role of neuronal coherence is unclear. Optogenetic stimulation allows causal tests of the functional significance of coherent neuronal activity. While non-human primates are important for studying the neural mechanisms of complex cognitive functions, optogenetic perturbation of neuronal dynamics has had limited application in this animal model. Here, we develop a computational framework and perform experiments to test how optogenetic stimulation perturbs coherent neuronal dynamics. We show that stimulation-evoked neural responses arise from temporal windows of excitatory and inhibitory activity that vary parametrically with optogenetic stimulation parameters. We experimentally identify the effective temporal window of excitation and inhibition and use the window in a computational model to design model-based stimulation sequences. These results demonstrate optogenetic perturbations of coherent neuronal dynamics and advance the use of optogenetic tools to study complex cognitive functions in the primate brain.

Introduction

Neurons dynamically coordinate their activity over a range of temporal frequencies across multiple scales, spanning individual neurons and neural populations[1]. Coherent neuronal dynamics capture neural coordination across multiple scales by measuring correlations between spiking activity of individual neurons and neural population activity, typically measured using local field potential (LFP) activity[2]. In the primate brain, the importance of coherent neuronal dynamics has been emphasized across a range of complex cognitive functions including working memory[3–5], decision making[6–8], coordination[9,10], attention[11,12], and perception[13,14]. While their precise function remains controversial[15], coherent neuronal dynamics at different frequencies in the beta (12-30 Hz) and gamma (30-100 Hz) bands are thought to play different functional roles[11]. To decisively test the role of coherent neuronal dynamics in complex cognitive functions, we need to be able to selectively manipulate temporally-patterned neuronal activity.

Optogenetic stimulation can perturb behavioral processes[16–18] and neuronal dynamics[19,20]. Early work tested predictions of computational models in which cell-type-specific manipulations underlie the impact of optogenetic stimulation on coherent neuronal dynamics. In some studies, driving interneurons using pulse trains of optogenetic stimulation perturbed coherent neuronal activity[20,21]. In other studies, driving pyramidal neurons using continuous optogenetic stimulation generated coherent dynamics, specifically gamma activity[22,23]. In each case, consistent with the cell-type specific models, the effect of optogenetic stimulation on coherent neuronal dynamics depends on which neurons have been transduced. Importantly, this work indicates that expression of different cell-type-specific optogenetic constructs is needed to perturb neuronal dynamics at different frequencies[20]. Thus, it is possible that neuronal coherence involves very specific effects in corresponding populations of cell-types across different cortical layers and areas. However, how to use optogenetic stimulation to

identify and compare specific functional roles for coherent neuronal dynamics at different frequency ranges remains unclear. If co-expression of multiple optogenetic tools with different patterns of transduction restricted to specific layers in a given brain region is required, identifying functional roles for different temporal patterns of activity will be particularly challenging, especially when studying complex cognitive functions in non-human primates.

In general, coherent neuronal dynamics are not simply due to laminar, cell-type specific mechanisms. Coherent neuronal dynamics also depend on the temporal precision and synchrony of spike timing, and the relative timing of post-synaptic excitatory (E) and inhibitory (I) responses[24,25]. Stimulating specific cell-types drives synaptically-mediated responses in a variety of cell-types present in the neuronal network[26–30]. As a result, how stimulation drives coherent neuronal dynamics depends on the relative timing of E-I responses. If so, this suggests that parameters for optogenetic stimulation pulse trains to generate a particular pattern of coherent neuronal dynamics can be selected in two complementary ways: 1 - how each stimulation pulse drives an effective temporal integration window of excitation and inhibition; and 2 – how sequences of stimulation pulses recruit relative timing of E-I responses appropriate to generating particular coherent neuronal dynamics.

Motivated by this reasoning, we tested the hypothesis that optogenetic stimulation can drive coherent neuronal dynamics at different frequencies by varying E-I responses and their relative timing through the choice of particular stimulation parameters. We first developed a computational model of coherent neuronal dynamics in response to optogenetic stimulation in terms of a temporal window of excitation and inhibition—the E-I window. Modeling the dynamic responses to optogenetic stimulation allowed us to choose the stimulation parameters—pulses and pulse sequences—appropriate to selectively perturb coherent activity in different frequency ranges. Consistent with previous work, the frequency of simulated coherent activity in the model depends on the relative timing of episodic E-I responses. The model also predicts that

optogenetic stimulation pulses and pulse sequences can be designed to shape synaptic excitation and inhibition and generate the desired coherent activity, allowing for model-based selection of stimulation parameters.

We experimentally tested the model predictions by expressing ChR2(H134R) in macaque cortex delivered by an AAV2/5 viral injection, and measuring spiking and local field potential (LFP) responses to optogenetic stimulation. We first examined the impact of altering the shape of the E-I window based on the stimulation pulse. We delivered a range of stimulation sequences with different pulse rates and pulse durations and examined driven coherent activity. We finish by considering the complementary manipulation of altering stimulation pulse sequences and present an experimental protocol for designing stimulation sequences that manipulate coherent neuronal dynamics. The results demonstrate how to generate coherent dynamics across frequencies in the beta and gamma bands according to model predictions. This study provides an approach to testing and comparing the causal role of different naturalistic coherent neuronal dynamics in computation and behavior.

Results

Modeling optogenetic-stimulation-evoked coherent neuronal dynamics. Spike-field coherence (SFC) measures coherent neuronal dynamics by estimating the strength of correlations between spiking activity of individual neurons and neural population activity in the form of simultaneously-recorded LFP activity. When the spike times of a neuron can be predicted from fluctuations in LFP activity at a particular frequency, the spiking is said to be coherent with LFP activity at that frequency. Neurons that fire consistently at a particular phase of LFP activity are coherent with LFP activity. In short, neuronal coherence is defined by coherent spiking and LFP activity and can be measured by estimating SFC between spiking and nearby LFP activity[2,3].

Figure 1 presents a model of optogenetic-stimulation-evoked coherent neuronal dynamics with the corresponding idealized neural responses. We model neuronal spiking according to a conditional intensity function where the probability of a spike occurring at time t is governed by an instantaneous firing rate $\lambda(t)$ that varies in time[31]. In the absence of optogenetic stimulation, we model background spiking activity as a Poisson process with a constant rate, λ_0 (**Fig. 1A**). We model background LFP activity as a process with increased power at low frequencies–"brown noise". For simplicity, we further assume that background LFP activity is uncorrelated with spiking activity and does not affect the value of $\lambda(t)$.

Direct activation of transduced neurons leads to excitatory and inhibitory synaptic currents within the local network of neurons. The resulting currents determine when neurons fire spikes. Excitatory currents lead neurons to fire spikes more frequently. Inhibitory currents lead neurons to fire spikes less frequently. Therefore, we model the impact of optogenetic stimulation on spiking as an excitatory- and inhibitory-dependent temporal change—an excitation-inhibition (E-I) window—in the spiking probability, $\lambda(t)$, in the conditional intensity function (**Fig. 1B**, Spike generation).

Since we do not have experimental access to the intracellular conductance changes in response to each stimulation pulse, we estimate the excitatory and inhibitory responses from the shape of the stimulation-evoked LFP. LFP activity predominantly reflects summed post-synaptic potentials[1,2]. Thus, the stimulation-triggered average LFP can reveal the temporal structure of windows of excitation and inhibition that arise from synaptic currents in the neural population[32,33]. Motivated by this, we model the stimulation-driven E-I response using the stimulation-triggered averaged LFP.

In the model, the E and I components are then summed to create the E-I window, which is convolved with a pulse train to model the combined E-I response to stimulation. To simulate spiking responses, the separate excitatory and inhibitory responses to the pulse train are passed through a non-linear transformation and summed to generate the time varying firing rate, $\lambda(t)$. Individual action potentials are randomly generated at each time point from a binomial random variable with $p(spike\ at\ time\ t) = \lambda(t)$. We separately model LFP activity in response to optogenetic stimulation as a linear sum of brown noise background activity and activity due to each stimulation pulse (**Fig. 1B**, LFP).

We refer to this model of neuronal coherence as the **E-I window model.** Since we model spontaneous spiking and LFP as uncorrelated, baseline activity does not contain SFC (**Fig. 1C**). Since optogenetic stimulation evokes E-I windows in which action potentials are more likely to occur, changes in spike probability are coupled to LFP responses. This coupling results in spikes that are coherent with LFP activity. The coherence is due to the temporal dynamics, or shape, of the E-I windows. (**Fig. 1D**).

Note that the neuronal coherence described by the E-I window model depends on predictability between spikes and LFP activity. This construction is consistent with but does not require invoking an oscillator or other phase-consistent process. This construction is also consistent with the use of SFC, as opposed to other metrics of phase consistency, to estimate coherent neuronal dynamics. This is because SFC measures predictability between spikes and LFP activity. Note also that our approach contrasts with previous work that has used cell-type-specific optogenetic stimulation to generate neuronal coherence.

Selectively generating coherent neuronal dynamics by varying E-I windows. According to the E-I window model, the frequency of coherent neuronal dynamics is determined by the E-I window. We first verified this prediction computationally by simulating the model. To

analyze the impact of E-I windows due to each stimulation pulse, we modelled E-I windows as a weighted sum of excitatory and inhibitory components

$$EI = \beta_{exc} exc - \beta_{inh} inh$$
$$exc = Ae^{-At}\left(\frac{(At)^{\alpha_{exc}}}{\alpha_{exc}!}\right)$$
$$inh = Ae^{-At}\left(\frac{(At)^{\alpha_{inh}}}{\alpha_{inh}!}\right)$$

where α_{exc} and α_{inh} govern the temporal dynamics of the excitatory and inhibitory components, respectively (**Fig. 2A**). To test how each stimulation pulse drives an effective E-I window that alters coherence, we simulated spiking and LFP activity while sweeping through values for the α_{exc} and α_{inh} parameters and used white noise Poisson stimulation pulse sequences. In our empirically measured E-I windows, excitatory responses dominated the early stage followed by inhibitory responses. This is consistent with sensory stimulation which typically generates an increase in excitation followed shortly by a corresponding inhibitory response[34,35]. However, inhibition may be stronger and have faster rise times than excitation in certain circuits or behaviors[36,37]. This regime would be captured in the E-I window model by setting $\alpha_{inh} > \alpha_{exc}$. In line with the prediction, the frequency content of SFC in the simulations varied with the E-I window duration (**Fig. 2B-C**). Longer E-I windows generated SFC at lower frequencies.

The influence of the E-I window on coherence was also present in the LFP activity alone. We defined a power spectral ratio (PSR) as the ratio of the driven LFP response to the baseline LFP response. The PSR captures the linearly-dependent influence of optogenetic stimulation on temporal structure in the neuronal activity. Consistent with SFC, the PSR also varies with E-I duration (**Fig. 2D-E**). Longer duration E-I windows drive increases in power at lower

frequencies. Since driven spiking activity may not be measured at all recording sites in an experiment, the results of the PSR analysis suggest LFP activity also could provide a robust indicator of the driven coherent dynamics.

Using both excitatory and inhibitory components to simulate stimulation responses provided a wide range of driven dynamics (**Fig. 2F**). Hence, the interaction between excitation and inhibition may allow for generating selective dynamics across a wider range of frequencies. Additional computational work suggested that the interplay of E- and I-windows was important to this result (**Supplementary Fig. 1**). Taken together, the simulation results suggest that coherent neuronal dynamics can be selectively generated using optogenetic stimulation to control E-I window durations, consistent with the E-I window model.

Optogenetic stimulation robustly generates frequency-selective responses. Next, we tested the E-I window model experimentally. The simulations suggested that varying the E-I window duration affects the frequency of driven coherent neuronal dynamics. This raised the question of how to experimentally vary the E-I window duration. We hypothesized that varying the duration of the stimulation pulse would drive different E-I windows, and thus alter the frequency content of the driven coherent neuronal activity.

To test this hypothesis, we injected AAV5-hSyn-ChR2(H134R)-EYFP and recorded neuronal responses in three alert macaque monkeys quietly seated in a primate chair. We recorded in the inferior and superior parietal lobules in Monkeys H and J and lateral to the post-central dimple in Monkey B (**Fig. 3A**)**.** We observed strong viral expression at each injection site with robust labelling of neurons and neuropil (**Fig. 3B**). We performed simultaneous *in vivo* optogenetic stimulation and recording using a fiber optic cable placed on a surgically thinned dura and adjacent to the intracortical recording electrode (**Fig. 3C**). Stimulation consisted of one second long sequences of light pulses (stimulation epoch) followed by 1-3 s of no stimulation

(baseline epoch) (**Fig. 3D**). Optogenetic stimulation reliably generated neural responses. These responses consisted of action potentials as well as large evoked field potentials visible on an individual pulse basis in the raw data (**Fig. 3E,F,G).**

We measured neuronal responses to stimulation sequences composed of Poisson pulse trains with different pulse rates and pulse durations. **Figure 4A** presents example neuronal responses during a stimulation block with 5 ms wide pulses delivered with a 20 pulse/s Poisson pulse train. Individual stimulation pulses drove spiking activity and evoked LFP responses at the stimulation site (**Fig. 4Ai,ii**). Stimulation drove spiking activity that was coherent with LFP activity at selective frequencies (**Fig. 4Aiii**). To quantify the response to the pulse train, we computed the power spectrum of LFP activity during the one second long stimulation epoch and one second prior to stimulation during the baseline epoch (**Fig. 4Aiv**). The peri-stimulation LFP power spectrum revealed a significant increase in power (Chi-squared test, $p<0.01$). The PSR shows that power is driven in a selective frequency range (**Fig. 4Av**).

Longer pulse durations generated longer duration changes in firing rate (**Fig. 4Bi**). Interestingly, LFP activity during wider pulses showed longer periods of excitation and inhibition (**Fig. 4Bii**). The longer-duration E-I window was associated with more selective changes in SFC and the LFP power spectrum (**Fig. 4Biii-v**). Therefore, stimulation sequences with different pulse durations can be used to selectively generate coherent neuronal dynamics, consistent with changing the E-I window duration. Thus, the E-I window model predicted the relationship between the E-I windows and the stimulation-evoked coherent neuronal dynamics.

Optogenetic stimulation generates pulse duration-dependent responses. We averaged SFC across a population of recording sites with driven spiking activity in response to stimulation using Poisson pulse trains with 5, 10, 15, and 20 ms duration pulses. SFC varied with pulse duration, consistent with the example site (**Fig. 4C**). In addition, we analyzed LFP

responses across recording sites with driven evoked potentials in the three animals for 2, 5, 8, 10, 12, 15, 18, and 20 ms duration pulses. As with the example site, the frequency content of the driven LFP varied with pulse duration across the population (**Fig. 4C**).

The frequency of driven coherence decreased with pulse duration ($r^2 = 0.88$, $p = 0.062$) (**Fig. 4C**, red). Consistent with the SFC, the frequency driven LFP response also depended on pulse duration ($r^2 = 0.60$, $p = 6.7\text{x}10^{-9}$) (**Fig. 4C**, black). Longer duration pulses drove more neuronal coherence at lower frequencies and did so in narrower bands ($r^2 = 0.36$, $p = 6.07\text{x}10^{-5}$) (**Fig. 4D**). Importantly the center frequency did not depend on the mean pulse rate for Poisson stimulation (**Supplementary Fig. 2**). The decoupling of frequency from pulse rate means that the amount of coherence can be controlled separately from the center frequency.

Overall, these results show that coherent neuronal dynamics in either beta or gamma frequency bands can be generated by stimulating the same population of neurons using stimulation pulses of different durations. Critically, the results did not require the need for transducing neurons in a cell-type-specific manner. The frequency content of the stimulation-driven coherence also appears similar to that of coherence observed during behavior. Beta band activity exists at a low frequency and in a narrow frequency band (12-30 Hz) compared to gamma band activity which is at a higher frequency and a wider frequency band (30-100 Hz).

E-I windows are site-specific. Figure 5 summarizes the experimental results. E-I windows also differ across stimulation sites, potentially due to variations in expression and local network properties (**Fig. 5A**). Hence at a single stimulation site, different pulse durations generate coherent neuronal activity at different frequencies, (**Fig. 5B,C**). However, **Fig 5D** illustrates how responses to the same pulse duration at other sites may differ. A short pulse at Site B could drive a narrower response, similar to **Fig. 5C**, but with different relative timing of

excitatory and inhibitory components. The different E-I timing results in coherent neuronal dynamics with different frequency structure.

Model-based generalization of local response dynamics. The presence of site-specific E-I windows suggests that in order to generate coherence in a frequency band of interest, the stimulation pulse train needs to be tailored to the E-I window at that site. However, empirically searching through the space of stimulation parameters at each site is time-consuming. This points to another potential advantage of the E-I window model: The model can be used to design stimulation sequences *in silico*. If so, empirically-derived responses from one set of parameters in the E-I window model could be used to estimate responses to other parameters.

To test whether a model-based procedure can select site-specific pulsatile stimulation parameters, we examined how stimulation parameters could be generalized across response sites. Using empirically-derived responses from one set of parameters in the E-I window model to estimate responses to other parameters allows for model-based, site-specific selection of pulsatile stimulation parameters. To do this, we temporally scaled the E-I response for a 10 ms pulse to provide an estimate of the temporal window of excitation to any arbitrary pulse duration (**Fig. 6A**). Scaling longer pulse durations, which have excitation windows that capture high frequency suppression, provides a better fit to experimental data than scaling shorter pulses (**Supplementary Fig. S3**). Performing simulations using the E-I window model with E-I windows that are temporally scaled versions of the experimental test condition produces a map that shows which frequencies can be generated using pulsatile Poisson stimulation (**Fig. 6B,** left). The E-I window model generates dynamics that match empirical results (**Fig. 6B**, left; black dots). Importantly, different pulse durations can be used to generate selective responses in bands typically associated with beta and gamma frequencies (**Fig. 6B,** right). The E-I window model also generates spiking that is coherent with LFP activity at beta and gamma frequencies

and varies with pulse width (**Fig. 6C**). The frequency content of the response is driven by parameter choice for the E-I window (**Fig. 6D**). This offers a way to separately test the contribution of each of these frequency bands to behavior.

Model-based prediction of responses when varying stimulation pulse sequences. In addition to changing the E-I window by varying the pulse duration, the frequency of driven coherent neuronal dynamics can be altered in a complementary manner by changing the temporal properties of the stimulation sequences. To generate narrow-band responses, we use a quasi-periodic stimulation pulse train where the probability of generating a stimulation pulse is given by $P(stim) = \beta(1+\alpha\sin(2\pi Ft))\Delta t$ (**Fig. 7A**). Periodic stimulation can also be used to generate narrow responses. However, periodic stimulation trains have power at the fundamental frequency and its harmonics, which can drive responses outside of the desired frequency (**Fig. 7B**). Quasi-periodic stimulation can reduce the stimulation harmonic content, while preserving the response at the frequency of interest leading to selective drive (**Fig. 7C**). Quasi-periodic stimulation robustly generates that frequency specificity on a trial-by-trial basis (**Fig. 7D**). Therefore, a quasi-periodic algorithm can generate frequency selective drive over short, behaviorally relevant periods of time.

Quasi-periodic stimulation offers other benefits. With periodic stimulation, increasing stimulation intensity by stimulating more frequently can also increase the frequency of driven responses. Quasi-periodic stimulation allows frequency-selective stimulation intensity to be controlled separately from the frequency of interest itself. Increasing the modulation depth, α, results in increased driven power and coherence around the frequency of interest and not at other frequencies (**Fig. 7E,F**). Changing the frequency of interest is achieved by varying F in order to generate a range of behaviorally relevant frequencies (**Fig. 7G, Supplementary Fig. 4**).

One concern highlighted by our results is that responses to square wave pulse trains have low power at nodes determined by the inverse of the pulse duration. These nodes occur where the stimulation sequence has no energy, at frequencies that are multiples of $\frac{1}{pulse\ width}$, as determined by the Fourier transform of a square wave. Since response linearity predicts that responses are shaped by the stimulation pulse shape, if the pulse shape has low power at a given frequency, then a periodic or quasi-periodic pulse train will not drive responses at that frequency (**Fig. 7G**, green). Conversely, if the pulse shape has a peak in power at a given frequency, then the response will be greater compared to stimulation at other desired frequencies with the same pulse duration (**Fig. 7G**, blue). To address this concern, we propose that the pulse duration should be chosen according to the desired response frequency (**Fig. 7H**).

Discussion

Here, we demonstrate that optogenetically-evoked neuronal coherence is consistent with the recruitment of a combination of excitatory and inhibitory responses leading to an effective temporal window for spiking–the E-I window. We use the E-I window model to parameterize stimulation sequences and show how the specific frequency of optogenetic stimulation-evoked coherence varies parametrically with stimulation parameters–pulse duration and sequence. Experimental results from optogenetically-stimulating non-human primate cortex confirmed model predictions and revealed that varying the pulse duration alters the stimulation driven E-I windows. These results are important because they show that varying optogenetic stimulation parameters alone can selectively generate coherent dynamics across a range of behaviorally relevant frequencies in the beta and gamma frequency bands by varying the effective E-I window.

Our work shows that pan-neuronal optogenetic stimulation generates E-I windows that drive coherent neuronal dynamics. The E-I window model contrasts with previous work that has used cell-type-specific optogenetic stimulation to generate neuronal coherence. That work suggests that activity in a single cell-type is necessary for driving coherence[19–22]. These ideas are not mutually exclusive. Direct stimulation of specific types of neurons recruits synaptically-mediated responses from other strongly connected neurons in the network[30]. This recruited ensemble shapes the frequency content of coherent neuronal dynamics[38]. Stimulation-evoked coherence measured under cell-type-specific optogenetic stimulation may also be designed according to an effective E-I window. Whether the E-I window model is as effective in predicting the impact of cell-type specific manipulations that target either E or I cells is an open question and will likely depend on the strength of recurrent connectivity in the network.

The E-I window model offers a mechanistic explanation for how E-I window-driven changes in spike timing affect driven coherent neuronal dynamics. The model makes use of an LFP-based conditional intensity function—the likelihood of spiking increases with excitation—to capture the E-I widow-dependence that couples spike timing and LFP activity. Since we defined coherent neuronal dynamics using SFC, LFP activity played a critical role in developing and fitting the E-I window model. LFP activity arises from synchronous neuronal activity that occurs due to temporally structured fluctuations of local excitation and inhibition[26,39,40]. Since the stimulation-evoked LFPs reveal the temporal structure of stimulation-induced post-synaptic potentials[32,33], we estimated the net E-I window in response to stimulation using LFP activity. Optogenetic stimulation couples spiking and LFP activity through the generation of E-I windows that increase the temporal precision of spike timing. Agreement between the model predictions and our empirical results demonstrates that using stimulation-evoked LFP activity is effective in capturing the phenomenology of the combined effect without relying on precise measurements of the E and I components. Therefore, the E-I window model captures the stimulation-driven E-I balance that controls spike timing.

The choice to use extracellular recordings for LFP activity and spiking may bias our measurements towards activity in pyramidal neurons. Due to the biophysics of extracellular potentials, LFP activity is most sensitive to post-synaptic potentials in neurons where the positive and negative current sources are separated to provide an open field geometry[2]. Thus, contributions from neurons with extended dendritic architectures, such as pyramidal neurons, are more heavily weighted by LFP activity. Additionally, pyramidal neurons typically have larger cell bodies than other cortical neurons and thus have more easily measurable action potentials. Therefore, our measurement of both spiking activity and LFP may be biased toward contributions from pyramidal neurons, thereby biasing our estimate of SFC toward the spiking that is coherent with post-synaptic potentials in pyramidal neurons. In addition to LFP activity,

alternative decompositions of neural data, such as projections of population activity onto lower dimensional subspaces, may be used to estimate coherence. Such estimates may be more effective at identifying spiking that is coherent with pre- and post-synaptic activity in neuronal ensembles containing both open and closed field neurons.

Other optogenetic stimulation sequences, such as continuous stimulation and periodic pulse sequence stimulation, have been used generate beta and gamma activity and study its effects on behavior without considering the E-I window dynamics[19–21,23,41]. These forms of stimulation have several limitations which we mitigate by controlling the properties of the stimulation pulse and stimulation sequence. The first limitation is that using continuous constant and pulsatile periodic stimulation drives responses at only particular frequencies. For example, continuous stimulation typically results in increased activity at some frequencies (e.g. gamma) and not others (e.g. beta)[19,20,22], presumably due to network-specific interactions[26]. Thus, the driven frequency may vary across brain regions and subjects[22,23] and these forms stimulation may not be able to flexibly generate activity in frequency bands of interest in a given experiment. We show that the frequency of driven coherent activity depends on the relative timing of episodic E-I responses. Controlling the E-I window timing by varying the stimulation pulse duration allows us to generate coherent activity across a broader range of behaviorally-relevant frequencies. Importantly, this allows us to use optogenetic stimulation to identify and compare specific functional roles for coherent neuronal dynamics at different frequency ranges without varying optogenetic construct expression.

The second limitation related to earlier work is that periodic pulsatile and continuous stimulation tend to generate oscillatory dynamics in narrow frequency band[19,20]. However, empirically observed coherent neuronal activity is not strictly oscillatory as oscillatory requires the presence of consistent phase relationships over extended time period[2,25,42,43]. Coherent neural activity is a broader term than oscillatory neural activity, only requires the presence of

statistically significant dependencies at specific frequency bands. Empirically observed neural coherence is dynamic and episodic, with fluctuations in phase and frequency, and can be narrow-band or broad-band. This is illustrated by, for example, the presence of a broad increase in LFP power across a range of frequencies instead of a narrow spectral peak. Therefore, while there is significant theoretical interest in neural oscillations, and previous work on optogenetic manipulations has focused on narrow-band manipulations using period and continuous stimulation, our contribution is to investigate and manipulate coherent neural activity patterns which are not necessarily oscillatory or narrow-band.

A related limitation is that in order to test the role of both broad-band and narrow-band activity in behavior, we need to be able to generate both within a single experiment. However, since periodic pulsatile and continuous stimulation tend to generate oscillatory dynamics in narrow frequency bands[19,20,23], they may not be effective for testing hypotheses about broad-band dynamics[42,43]. Another important limitation we mitigate is that periodic stimulation has power at harmonic frequencies, which can drive responses outside of the desired frequency range and confound results. We show that the choice of stimulation pulse sequence can alter the bandwidth of driven coherence. Poisson pulsatile stimulation generates episodic coherent neuronal dynamics with broader spectral peaks, rather than more oscillatory, narrow-peaked responses (**Fig 4Aiii,Biii**). On the other hand, quasi-periodic stimulation drives narrow-peaked responses with minimal coherent activity at harmonic frequencies compared to periodic stimulation (**Fig. 7B,C**). The E-I window model predicts how the parameters optogenetic stimulation pulses and sequences can be selected to shape synaptic excitation and inhibition and generate the desired coherent neuronal dynamics. This model-based approach to parameter selection mitigates the need for time-consuming empirical searching through the space of stimulation parameters.

A final limitation is that continuous stimulation can introduce confounds due to tissue heating[44]. Extended periods during which the light is on may affect the neural response properties to changes in the temperature of the tissue, rather than neuronal mechanisms. In addition, this heating may cause tissue damage over repeated stimulation. However, we show that a range of frequencies can be driven using pulsatile stimulation, which decreases the duty cycle and minimizes tissue heating.

Are forms of stimulation other than optogenetic stimulation useful for studying coherent neuronal dynamics and behavior? Electrical and magnetic stimulation approaches have been used to precisely generate temporal structure in neuronal activity[45–48] and study the impact of temporally patterned stimulation on behavior[49,50]. However, a significant difficulty in interpreting the results of causal manipulations is that stimulating neuronal networks can lead to a variety of non-linear and dynamic response properties in addition to coherent dynamics[51–53]. This is particularly difficult for electrical stimulation due to the likelihood of activating fibers of passage in addition to cell bodies. Consequently, the mechanistic interpretation of the effects of stimulation is unclear and simultaneous recordings of neuronal activity during stimulation are needed to confirm the impact of stimulation sequences on coherent neuronal dynamics as opposed to other features of the neuronal responses. Sequences of electrical and magnetic stimulation pulses can generate substantial recording artifacts that are difficult to suppress, especially for field potentials, obscuring responses and introducing significant confounds[54,55]. Our results show that, unlike electrical or magnetic stimulation, optogenetic stimulation can be interpreted in a model-based framework and used in a manner that introduces few, if any, artifacts to simultaneous electrophysiological recordings and allows us to control for non-linear and dynamic response properties.

In conclusion, we systematically modeled neuronal responses to optogenetic stimulation in non-human primate frontal cortex. We highlight the role of selecting stimulation parameters—

pulses and pulse sequences—to generate E-I windows and selectively perturb coherent neuronal activity. Importantly, we do so without necessarily targeting optogenetic expression to specific types of neurons. In general, our results show that combining experimental measures with model-based predictions can be used to study how optogenetic stimulation drives network dynamics across a wide range of experimental designs, including using different brain regions, model species, and stimulation protocols. These results demonstrate that the ability to selectively generate episodic dynamics in behaviorally-relevant frequency ranges in the primate brain can be useful for understanding how coherent neuronal dynamics give rise to complex, flexible behaviors.

Methods:

Animals

Recordings were taken from two male rhesus macaques (*Macaca mulatta*) (Monkey J: 12 years, 6.5 kg; Monkey H: 11 years, 10.5 kg) and one male cynomolgus macaque (*Macaca fascicularis*) (Monkey B: 4 years, 5 kg). Monkeys J and H had been part of previous studies using the contralateral intraparietal sulcus and the ipsilateral frontal cortex. Monkey B had not been part of previous experiments. All animals were in normal health and were group housed with other conspecifics at the facility. All surgical and animal care procedures were approved by the New York University Animal Care and Use Committee and were performed in accordance with the National Institute of Health guidelines for care and use of laboratory animals.

Injection surgery

We performed injections of optogenetic viral vectors 6-25 weeks prior to recording. Subjects were maintained at a constant depth of anesthesia with isofluorane (1-2%). Monkey J and H were injected in existing craniotomies. In Monkey B, after mobilizing the scalp and other soft tissue, we made craniotomies over motor cortex to provide access for injections. Injections were made through 26 s gauge stainless steel cannulas (Hamilton) that were inserted through a thinned dura. For each injection, one microliter of AAV5-hSyn-ChR2(h134R)-EYFP was injected at a rate of 0.05 μl/min. We made injections at 2-3 depths spaced 500-750 μm across 2-4 cortical sites per animal. We injected at multiple sites simultaneously to increase total number of injections sites and thus increase the probability of having successful transduction at one or more sites. We waited 20 minutes between each injection to allow for the virus to diffuse through the tissue. After injections, chambers were reclosed with the chamber cap and periodically opened for cleaning and maintenance while the viral vector was expressing.

Optical Stimulation

We illuminated the injection site with a 473 nm Laser (Shanghai Sanctity Laser) connected to a multi-mode fiber optic cable (200 μm core, BFL-200, Thor Labs). One end of the fiber optic cable was terminated with an FC/PC connecter and connected to a collimator (PAFA-X-4-A, Thor Labs) for focusing light from the laser. At the other end of the cable we removed a small amount of buffer with a microstripper (T12S21, Thor Labs) and cleaved it with a diamond knife (S90R, Thorlabs) to ensure a flat edge for minimal power-loss.

The fiber optic was placed on top of the thinned dura. The cable was held in the microdrive and placed in the same guide tube as the recording electrode. We did not insert the fiber into the brain in order to minimize damage to the neural tissue. Light power at the tip varied from 16-20.5 mW. (510-653 mW/mm^2), as measured prior to each experiment using a power meter (PM100D, Thor Labs). Evoked potentials were visually inspected to ensure that there were no signs of artifacts from the Becquerel effect, including rapid onset or offset of neural responses locked to the timing of the light[56]. Light based artifacts typically have a capacitive charging and discharging profile, which has a rapid onset and offset tightly coupled to the onset and offset of the device. We ensured that the onset of the response and the inflection point were not aligned with the times when the light was turned on and off. The neural response is slower than the duration of the light pulse and thus continues to increase for a brief period after the light has been turned off. The onset is delayed because the ChR2 channel dynamics are slower than the chemical response and thus the membrane potential does not start to change immediately. The initial response recruits network activity, which has a slow time course. This is particularly evident for short light pulses (<=5 ms). When there is no artifact, the response inflection point occurs after the light is turned off. This is less clear for longer pulse widths (>15 ms) because adaptation and other properties of channel kinetics can lead to a decrease in the response prior to the end of stimulation.

Light pulse patterns were generated by proprietary software running in LabVIEW (National Instruments) and converted to analog signals using a DAQ card (USB-6251, National Instruments). Stimulation trials consisted of 1 s long bursts of square wave pulses. For each block of trials, we controlled three stimulation parameters: pulse width, pulse rate and pulse distribution. We varied pulse widths from 1-20 ms, pulse rates from 5-80 Hz and used both Poisson and periodic pulse distributions.

In rodents, both measurement and simulation have proposed that ~1% of light power density remains after light has passed through approximately 1 mm of brain tissue[57–59]. However, primate brain tissue may have slightly different optical properties, thus altering the light transmission. In addition, we stimulated transdurally which may have additional effects on the light. However, we were able to record purportedly directly driven spiking (low-latency, low-jitter) as far as 1.5mm below the cortical surface (not shown), suggesting that we were activating neurons into layer 3.

We tested each recording site in pseudo-randomly interleaved blocks of recordings. Each block consisted of 30-60 repetitions of 1 s long sequences of square wave pulses (bursts), with 1-3 s of no stimulation between each stimulation burst (**Fig 3C**). We held other stimulation parameters (pulse rate, duration and intensity) constant within each block.

Poisson and periodic stimulation pulse trains were generated *in silico* using the same pulse width and rate parameters. Simulations consisted of 1000 trials for each combination of parameters.

Electrophysiology

We recorded neural signals from awake, alert macaques while they were seated, head-fixed in a primate chair (Rogue Research) in a dark, quiet room. Neural signals were recorded on glass-coated tungsten electrodes (Alpha-Omega, impedance: 0.7-0.8 MΩ at 1 kHz) held in a FlexMT microdrive (Alpha Omega). Neural signals were acquired at 30 kHz on an NSpike DAQ

system and recorded using proprietary data acquisition software. Neural recordings were referenced to a metal wire placed in contact with the dura and away from the recording site. We recorded from one site in monkey B (pre-motor cortex) and three sites in each Monkeys J and H (parietal cortex). We recorded driven LFP activity at all sites and driven multi-unit activity at one site in each subject.

Fitting E-I Windows

E-I windows were fit to the form

$$EI = Ae^{-At}\left(\frac{\beta_{exc}\left(At\right)^{\alpha_{exc}}}{\alpha_{exc}!} - \frac{\beta_{inh}\left(At\right)^{\alpha_{inh}}}{\alpha_{inh}!}\right)$$

which has an excitatory component

$$E = Ae^{-At}\left(\frac{\beta_{exc}\left(At\right)^{\alpha_{exc}}}{\alpha_{exc}!}\right)$$

and an inhibitory component

$$I = Ae^{-At}\left(\frac{\beta_{inh}\left(At\right)^{\alpha_{inh}}}{\alpha_{inh}!}\right).$$

For the pure simulations, A, β_{exc} and β_{inh} were set to 1. To fit empirical E-I windows, all parameters were fit using a grid search to minimize the squared error between the modelled window and the empirical window.

E-I Window Model

To simulate LFPs using a excitation window model, we generated $\frac{T}{dt}$ samples of Brownian noise as background activity, with T =1 s and dt =1 ms. We estimated an E-I window for each recording site by fitting the stimulation pulse evoked LFP response to the following model:

$$EI = \beta_{exc} exc - \beta_{inh} inh$$
$$exc = Ae^{-At}\left(\frac{(At)^{\alpha_{exc}}}{\alpha_{exc}!}\right)$$
$$inh = Ae^{-At}\left(\frac{(At)^{\alpha_{inh}}}{\alpha_{inh}!}\right)$$

For excitatory- and an inhibitory-only simulations, β_{inh} and β_{exc} were set to zero, respectively. We simulated the driven LFP by convolving the site-specific E-I window with a sequence of delta pulses determined by the stimulation parameters. The driven LFP was and added to the background activity to generate the total simulated LFP activity.

We modelled spiking activity that was coherent with the LFP using a Poisson point process with a conditional intensity function. The conditional intensity function models stochastic spiking governed by a time-varying instantaneous firing rate modelled as

$$\lambda(t) = (\lambda_E(t) + \lambda_I(t) + \lambda_0) \cdot dt$$
$$\lambda_E(t) = f(E(t)) = e^{E(t)}$$
$$\lambda_I(t) = g(I(t)) = e^{I(t)}$$

where λ_0 is the baseline firing rate, and dt is the sampling rate. $E(t)$ and $I(t)$ are the time courses of optogenetically driven E and I response, respectively, that generate the fluctuations in the conditional intensity function, $\lambda(t)$. $E(t)$ and $I(t)$ is determined by convolving the E-I window with a Poisson process generated from the stimulus sequence parameters, then positively or negatively rectifying the E-I response to get the separate E and I responses. After a spike we used a fixed refractory period by forcing $\lambda(t) = 0$ for 3ms.

Simulations of the excitation window model were run using custom scripts in MATLAB using a 1 ms time step. For each trial, we simulated 1 s of baseline activity and 1 s of stimulation. We simulated 1000 trials for set of stimulus parameters.

Pre-processing in vivo data

Broad-band neural activity was split into multi-unit signals and local field potentials (LFP) by high-pass and low-pass filtering, respectively, at 300 Hz. LFP signals were down-sampled to 1 kHz. Multi-unit activity (MUA) was computed by applying a 3.5 standard deviation threshold to the multi-unit signals to identify putative spikes. All waveforms that exceeded this peak were labelled as multi-unit action potentials.

Data Analysis

We computed multi-unit peri-stimulus time histograms (PSTH) by aligning MUA to the onset time of light pulses. Individual spikes were collected in 1 ms bins and the corresponding histogram was smoothed by convolution with a Gaussian function with a standard deviation of 1 ms. In order to avoid corruption from nearby pulses, evoked potentials were computed by averaging LFPs aligned to the onset time of light pulses only for pulses that occurred at the end of a pulse train and did not have a pulse preceding it by less than 50 ms.

Spectral analysis was performed using multi-taper methods [60]. The accuracy of the spectral quantities we used does not depend on the center frequency of the estimate for all frequencies above the minimum resolvable frequency, given by the frequency smoothing in Hz[61]. For each recording, power spectra were computed using a 1 s analysis window and ± 1.5 Hz frequency smoothing. We computed power spectra for the LFP responses during entire 1 s burst (stimulation epoch) and for 1 s prior to the burst (baseline epoch). Power spectra were computed for neural signals for the baseline and stimulation epochs. Recording sites that did not exhibit a significant difference in were not included in analysis. The exclusion criteria for recording sessions did not depend on the frequency content of the driven LFP response—the desired effect—but rather only that there was any driven LFP response at all. Sites were excluded if there was no change in the LFP power between baseline and stimulation periods for the 10ms pulse width condition, which was likely due to the electrode being placed on the periphery of light cone and thus failing to record driven neural activity. We explicitly confirm this

in our experiments by moving the electrode and observing driven responses. We computed the spectrogram for each recording using a ± 250 ms analysis window, stepped 50 ms between windows, with ± 2.5 Hz frequency smoothing aligned to the start of the burst. We computed the spike-field coherence for each recording using a 1 s analysis window with ± 3 Hz frequency smoothing averaged across at least 30 repetitions.

Power Spectral Ratio

We also computed a spectral ratio by dividing each of these power spectra by the baseline power spectrum of the neural response. In typical linear systems analysis, the dynamical system is quiescent unless driven by input. However, spontaneous neural activity is present *in vivo*. Therefore, to understand the impact of stimulation the analysis needs to account for the presence of ongoing neural activity. We modeled the recorded neural activity during stimulation, $y(t)$, as a sum of the ongoing spontaneous activity $s(t)$, and the stimulation response $T\left[u(t)\right]$, where T is the transfer function of the neural system and $u(t)$ is the stimulus input.

$$y(t) = s(t) + T\left[u(t)\right] \tag{1}$$

Due to the linearity of the Fourier transform, we can rewrite this equation in the Fourier domain as

$$Y(f) = S(f) + H(f)U(f) \tag{2}$$

We then quantified the effects of stimulation on LFP power by computing an index given by the ratio of peri-stimulation power to baseline power. Since the ongoing activity spectrum, $S(f)$, can be estimated as the baseline LFP power spectrum, the spectral ratio is approximately proportional to the effect of stimulation without ongoing activity

$$SpectralRatio = \frac{Y(f)}{S(f)} = \frac{S(f) + H(f)U(f)}{S(f)} \tag{3}$$

$$SpectralRatio = 1 + \frac{H(f)U(f)}{S(f)} \tag{4}$$

$$SpectralRatio - 1 \propto H(f)U(f) \tag{5}$$

For the example recording, we can naively predict the neural response as a sum of spontaneous activity and a linear response to the pulse train

$$Y_p(f) = S(f) + aX(f) \tag{6}$$

where a is a scaling factor. The power ratio for the predicted response is proportional to the spectrum of the stimulus.

$$SpectralRatio = \frac{Y_p(f)}{S(f)} = \frac{aX(f)}{S(f)} + 1 \tag{7}$$

$$SpectralRatio - 1 \propto X(f) \tag{8}$$

Power spectral ratios for the neural data for each recording were fit using a sum of Gaussians model, in order to identify the peaks and widths of the power increases. This was done using the peakfit.m MATLAB function[62] with Gaussian functions used to model the peaks. Each fitted Gaussian has two parameters, the mean and standard deviation, so we collected these for the components of the model for each recording. The mean was used to measure the frequency of a peak of an increase in the power spectrum, while the standard deviation provided an estimate of the width of the power that was increased.

DATA AND SOFTWARE AVAILABILITY

Software is available in a GitHub repository linked from http://www.pesaranlab.org. Data are available upon reasonable request.

Acknowledgements:

This work was supported, in part, by US National Institutes of Health (NIH) BRAIN Initiative grant R01-NS104923, NIH R01-EY024067, NIH P30-EY013079, NIH Training Grant T32-EY007136, a Scholar Award from the McKnight Endowment Fund for Neuroscience (BP) and the Alfred P Sloan Foundation (BP).

Author Contributions:

Conceptualization: R.A.S., H.L.D., Y.T.W., M.A.H., and B.P.; Methodology: R.A.S., H.L.D., Y.T.W., M.A.H., M.M.F. and B.P.; Software: R.A.S., H.L.D., and B.P.; Formal Analysis: R.A.S. and B.P.; Investigation: R.A.S. and B.P.; Resources: R.A.S., H.L.D., and B.P.; Writing – Original Draft: R.A.S. and B.P.; Writing – Review & Editing: R.A.S., H.L.D., Y.T.W., M.A.H., M.M.F. and B.P.; Visualization: R.A.S. and B.P.; Supervision: H.L.D., Y.T.W., M.A.H., and B.P.; Funding Acquisition: B.P.

Competing Financial Interests:

The authors declare no competing financial interests.

References

1. Buzsáki, G., Anastassiou, C. A. & Koch, C. The origin of extracellular fields and currents — EEG, ECoG, LFP and spikes. *Nat. Rev. Neurosci.* **13,** 407–420 (2012).
2. Pesaran, B. *et al.* Investigating large-scale brain dynamics using field potential recordings: analysis and interpretation. *Nat. Neurosci.* (2018). doi:10.1038/s41593-018-0171-8
3. Pesaran, B., Pezaris, J. S., Sahani, M., Mitra, P. P. & Andersen, R. A. Temporal structure in neuronal activity during working memory in macaque parietal cortex. *Nat. Neurosci.* **5,** 805–811 (2002).
4. Salazar, R. F., Dotson, N. M., Bressler, S. L. & Gray, C. M. Content-Specific Fronto-Parietal Synchronization During Visual Working Memory. *Science (80-.).* **1097,** (2012).
5. Siegel, M., Warden, M. R. & Miller, E. K. Phase-dependent neuronal coding of objects in short-term memory. *Proc. Natl. Acad. Sci. U. S. A.* **106,** 21341–21346 (2009).
6. Pesaran, B., Nelson, M. J. & Andersen, R. a. Free choice activates a decision circuit between frontal and parietal cortex. *Nature* **453,** 406–9 (2008).
7. Hawellek, D. J., Wong, Y. T. & Pesaran, B. Temporal coding of reward-guided choice in the posterior parietal cortex. *Proc. Natl. Acad. Sci.* **113,** 13492–13497 (2016).
8. Wong, Y. T., Fabiszak, M. M., Novikov, Y., Daw, N. D. & Pesaran, B. Coherent neuronal ensembles are rapidly recruited when making a look-reach decision. *Nat. Neurosci.* **19,** 1–11 (2016).
9. Hagan, M. A., Dean, H. L. & Pesaran, B. Spike-field activity in parietal area LIP during coordinated reach and saccade movements. *J. Neurophysiol.* **107,** 1275–1290 (2012).
10. Dean, H. L., Hagan, M. A. & Pesaran, B. Only Coherent Spiking in Posterior Parietal Cortex Coordinates Looking and Reaching. *Neuron* **73,** 829–841 (2012).

11. Buschman, T. J. & Miller, E. K. Top-down versus bottom-up control of attention in the prefrontal and posterior parietal cortices. *Science* **315,** 1860–2 (2007).

12. Gregoriou, G. G., Gotts, S. J., Zhou, H. & Desimone, R. High-Frequency, Long-Range Coupling Between Prefrontal and Visual Cortex During Attention. **324,** 1207–1211 (2009).

13. Gray, C. M., König, P., Engel, A. K. & Singer, W. Oscillatory responses in cat visual cortex exhibit inter-columnar synchronization which reflects global stimulus properties. *Nature* **338,** 334–337 (1989).

14. Womelsdorf, T., Fries, P., Mitra, P. P. & Desimone, R. Gamma-band synchronization in visual cortex predicts speed of change detection. *Nature* **439,** 733–736 (2006).

15. Uhlhaas, P. J. *et al.* Neural synchrony in cortical networks: history, concept and current status. *Front. Integr. Neurosci.* **3,** 17 (2009).

16. Dai, J., Brooks, D. I. & Sheinberg, D. L. Optogenetic and electrical microstimulation systematically bias visuospatial choice in primates. *Curr. Biol.* **24,** 63–69 (2014).

17. Jazayeri, M., Lindbloom-Brown, Z. & Horwitz, G. D. Saccadic eye movements evoked by optogenetic activation of primate V1. *Nat. Neurosci.* **15,** 1368–1370 (2012).

18. Stauffer, W. R. *et al.* Dopamine Neuron-Specific Optogenetic Stimulation in Rhesus Macaques. *Cell* **166,** 1564–1571.e6 (2016).

19. Adesnik, H. & Scanziani, M. Lateral competition for cortical space by layer-specific horizontal circuits. *Nature* **464,** 1155–1160 (2010).

20. Cardin, J. a *et al.* Driving fast-spiking cells induces gamma rhythm and controls sensory responses. *Nature* **459,** 663–7 (2009).

21. Sohal, V. S., Zhang, F., Yizhar, O. & Deisseroth, K. Parvalbumin neurons and gamma rhythms enhance cortical circuit performance. *Nature* **459,** 698–702 (2009).

22. Lu, Y. *et al.* Optogenetically induced spatiotemporal gamma oscillations and neuronal spiking activity in primate motor cortex. *J. Neurophysiol.* **113,** 3574–3587 (2015).

23. Ni, J. *et al.* Gamma-Rhythmic Gain Modulation. *Neuron* **92,** 240–251 (2016).

24. Gabernet, L., Jadhav, S. P., Feldman, D. E., Carandini, M. & Scanziani, M. Somatosensory integration controlled by dynamic thalamocortical feed-forward inhibition. *Neuron* **48,** 315–27 (2005).

25. Chariker, L., Shapley, R. & Young, L.-S. Rhythm and Synchrony in a Cortical Network Model. *J. Neurosci.* **38,** 8621–8634 (2018).

26. Buzsáki, G. & Wang, X.-J. Mechanisms of Gamma Oscillations. *Annu. Rev. Neurosci.* **35,** 203–225 (2012).

27. Gloveli, T. *et al.* Differential involvement of oriens/pyramidale interneurones in hippocampal network oscillations in vitro. *J. Physiol.* **562,** 131–147 (2005).

28. Pike, F. G. *et al.* Distinct frequency preferences of different types of rat hippocampal neurones in response to oscillatory input currents. *J. Physiol.* **529,** 205–213 (2000).

29. Tukker, J. J., Fuentealba, P., Hartwich, K., Somogyi, P. & Klausberger, T. Cell Type-Specific Tuning of Hippocampal Interneuron Firing during Gamma Oscillations In Vivo. *J. Neurosci.* **27,** 8184–8189 (2007).

30. Phillips, E. A. K. & Hasenstaub, A. R. Asymmetric effects of activating and inactivating cortical interneurons. *Elife* **5,** 1–22 (2016).

31. Brown, E. N., Barbieri, R., Eden, U. T. & Frank, L. M. in *Computational Neuroscience: A Comprehensive Approach* (ed. Feng, J.) 253–286 (CRC Press, 2003).

32. Poulet, J. F. A. & Petersen, C. C. H. Internal brain state regulates membrane potential synchrony in barrel cortex of behaving mice. *Nature* **454,** 881–885 (2008).

33. Okun, M., Naim, A. & Lampl, I. The Subthreshold Relation between Cortical Local Field Potential and Neuronal Firing Unveiled by Intracellular Recordings in Awake Rats. *J. Neurosci.* **30,** 4440–4448 (2010).

34. Wehr, M. & Zador, A. M. Balanced inhibition underlies tuning and sharpens spike timing in auditory cortex. *Nature* **426,** 442–446 (2003).

35. Higley, M. J. & Contreras, D. Nonlinear integration of sensory responses in the rat barrel

cortex: an intracellular study in vivo. *J. Neurosci.* **23,** 10190–200 (2003).

36. Cruikshank, S. J., Urabe, H., Nurmikko, A. V. & Connors, B. W. Pathway-Specific Feedforward Circuits between Thalamus and Neocortex Revealed by Selective Optical Stimulation of Axons. *Neuron* **65,** 230–245 (2010).

37. Haider, B., Häusser, M. & Carandini, M. Inhibition dominates sensory responses in the awake cortex. *Nature* **493,** 97–100 (2013).

38. Kato, H. K., Asinof, S. K. & Isaacson, J. S. Network-Level Control of Frequency Tuning in Auditory Cortex. *Neuron* **95,** 412–423.e4 (2017).

39. Csicsvari, J., Jamieson, B., Wise, K. D. & Buzsáki, G. Mechanisms of gamma oscillations in the hippocampus of the behaving rat. *Neuron* **37,** 311–322 (2003).

40. Hasenstaub, A. *et al.* Inhibitory postsynaptic potentials carry synchronized frequency information in active cortical networks. *Neuron* **47,** 423–435 (2005).

41. Tchumatchenko, T., Newman, J. P., Fong, M. & Potter, S. M. Delivery of continuously-varying stimuli using channelrhodopsin-2. *Front. Neural Circuits* **7,** 184 (2013).

42. Xing, D. *et al.* Stochastic Generation of Gamma-Band Activity in Primary Visual Cortex of Awake and Anesthetized Monkeys. *J. Neurosci.* **32,** 13873–13880a (2012).

43. Burns, S. P., Xing, D. & Shapley, R. M. Is gamma-band activity in the local field potential of V1 cortex a ‘clock’ or filtered noise? *J. Neurosci.* **31,** 9658–9664 (2011).

44. Stujenske, J. M., Spellman, T. & Gordon, J. A. Modeling the Spatiotemporal Dynamics of Light and Heat Propagation for In Vivo Optogenetics. *Cell Rep.* **12,** 525–534 (2015).

45. Casarotto, S. *et al.* EEG responses to TMS are sensitive to changes in the perturbation parameters and repeatable over time. *PLoS One* **5,** (2010).

46. Radman, T., Su, Y., An, J. H., Parra, L. C. & Bikson, M. Spike timing amplifies the effect of electric fields on neurons: implications for endogenous field effects. *J. Neurosci.* **27,** 3030–6 (2007).

47. Schmidt, S. L., Iyengar, A. K., Foulser, A. A., Boyle, M. R. & Fröhlich, F. Endogenous

cortical oscillations constrain neuromodulation by weak electric fields. *Brain Stimul.* **7,** 878–89 (2014).

48. Choi, J. S. *et al.* Eliciting naturalistic cortical responses with a sensory prosthesis via optimized microstimulation. *J. Neural Eng.* **13,** 056007 (2016).

49. Bari, B. A., Ollerenshaw, D. R., Millard, D. C., Wang, Q. & Stanley, G. B. Behavioral and electrophysiological effects of cortical Microstimulation parameters. *PLoS One* **8,** 1–13 (2013).

50. Van Acker, G. M. *et al.* Effective intracortical microstimulation parameters applied to primary motor cortex for evoking forelimb movements to stable spatial end points. *J. Neurophysiol.* **110,** 1180–9 (2013).

51. Millard, D. C., Wang, Q., Gollnick, C. A. & Stanley, G. B. System identification of the nonlinear dynamics in the thalamocortical circuit in response to patterned thalamic microstimulation in vivo. *J. Neural Eng.* **10,** 066011 (2013).

52. Nassi, J. J., Avery, M. C., Cetin, A. H., Roe, A. W. & Reynolds, J. H. Optogenetic Activation of Normalization in Alert Macaque Visual Cortex. *Neuron* **86,** 1504–17 (2015).

53. Muldoon, S. F. *et al.* Stimulation-Based Control of Dynamic Brain Networks. *PLoS Comput. Biol.* **12,** (2016).

54. Olsson, R. H., Buhl, D. L., Sirota, A. M., Buzsaki, G. & Wise, K. D. Band-tunable and multiplexed integrated circuits for simultaneous recording and stimulation with microelectrode arrays. *IEEE Trans. Biomed. Eng.* **52,** 1303–11 (2005).

55. Mueller, J. K. *et al.* Simultaneous transcranial magnetic stimulation and single-neuron recording in alert non-human primates. *Nat. Publ. Gr.* **17,** 1130–1136 (2014).

56. Cardin, J. a *et al.* Targeted optogenetic stimulation and recording of neurons in vivo using cell-type-specific expression of Channelrhodopsin-2. *Nat. Protoc.* **5,** 247–254 (2010).

57. Aravanis, A. M. *et al.* An optical neural interface: in vivo control of rodent motor cortex with integrated fiberoptic and optogenetic technology. *J. Neural Eng.* **4,** S143-56 (2007).

58. Yizhar, O., Fenno, L. E., Davidson, T. J., Mogri, M. & Deisseroth, K. Optogenetics in neural systems. *Neuron* **71,** 9–34 (2011).

59. Huber, D. *et al.* Sparse optical microstimulation in barrel cortex drives learned behaviour in freely moving mice. *Nature* **451,** 61–4 (2008).

60. Mitra, P. P. & Pesaran, B. Analysis of dynamic brain imaging data. *Biophys. J.* **76,** 691–708 (1999).

61. Jarvis, M. R. & Mitra, P. P. Sampling properties of the spectrum and coherency of sequences of action potentials. *Neural Comput.* **13,** 717–49 (2001).

62. O'Haver, T. A Pragmatic Introduction to Signal Processing. *Univ. Maryl. Coll. Park* 1–121 (2014).

Figure Legends

Figure 1. Excitation and inhibition drive coherent neuronal dynamics. (A) During spontaneous activity, synaptic inputs drive activity in a local network. We model spiking as being generated from a Poisson process with a constant rate and LFP as being generated from a Brown noise process. Under these assumptions, spontaneous spiking is not coherent with spontaneous LFP**. (B)** To model of optogenetic stimulation of a population of transduced neurons, we simulated pulsatile responses generated by direct activation of ChR2 channels and synaptic activity. Pulsatile responses are convolved with a stimulation sequence. The summed excitatory and inhibitory (E-I, black) components comprise the simulated LFP. The individual E (blue) and I (red) activity govern the variable spiking rate in the Poisson process which generates coherent spiking. **(C)** Spontaneous activity in the model has no spike-field coherence. **(D)** Optogenetic stimulation drives correlated fields and spiking, leading to frequency selective spike-field coherence.

Figure 2. E-I window shape controls frequency of coherent activity. (A) Excitation, inhibition and E-I windows generated when varying α_{exc} and setting $\alpha_{inh} = \alpha_{exc} + 1$ to alter the duration of the windows. E-I is the sum of E and I windows. **(B)** Spike-field coherence that results from using the E-I windows from (A) in the model. E-I duration is measured as the time from the onset of the response and when the response returns to the stable state. **(C)** Example coherence for various E-I windows in (B). **(D)** Power spectral ratio that results from using the E-I windows from (A) in the model. **(E)** Example PSRs for various E-I windows in (D). **(F)** Right, frequency of peaks in the SFC (blue) and PSR (red) for each E-I window in (A).

Figure 3. Optogenetic stimulation in macaque cortex. (A) Recording locations in all animals. The area of the circle corresponds to the number of sites recorded in each animal. **(B)** Example

injection site with YFP labeled neurons and neuropil from horizontal section. Inset: image of a single transduced neuron. **(C)** Recordings were performed with a single, acute electrode during trans-dural light stimulation with a fiber optic place over a surgically thinned dura. **(D)** Experimental design featured a 1 s stimulation pulse sequence followed by 1-3 s without stimulation. **(E)** Example raster plot (top) and PSTH (bottom) of the spiking response triggered on each stimulation pulse for Poisson distributed trains of 1 ms pulses at 10 pulse/s rate. **(F)** Example broadband recording during a pulse train containing 1 ms pulses at 10 pulse/s rate; optogenetic stimulation (blue). Inset: Response to a single pulse. **(G)** Example multiunit filtered data from (E). Inset: Stimulation-elicited spike.

Figure 4. Neuronal dynamics driven by optogenetic stimulation. (A) Neuronal responses to 5 ms pulse duration, 20 Hz pulse rate, periodic pulse train. (i) Raster (top) and PSTH (bottom) of the response to single light pulses (blue). (ii) Mean evoked potential for all the stimulation pulses that were the last in a sequence and not preceded by a prior stimulation pulse within 50 ms, normalized by subtracting the value of the LFP at the onset of the light. Dotted line indicates 0 mV. (iii) Spike-field coherence for multi-unit activity and LFP measured on the same electrode. Dotted horizontal line shows expected coherence under the null hypothesis that coherence is zero. (iv) Power spectral density (PSD) of 1 s of data during stimulation (black line) and spontaneous activity prior to stimulation (grey line). The dotted lines are error bars determined by the Chi-squared test for $p=0.01$. Solid gray lines above the PSD illustrate frequency bands where the stimulus PSD was significantly different from the spontaneous PSD ($p<0.01$). (v) Power spectral ratio showing frequency specific increases in power due to stimulation. **(B)** Same as (A) for 20 ms, 20 pulses/s pulse rate, Poisson pulse train. **(C)** Population mean of peak frequency for the SFC (red) and PSR (black) for each pulse duration across the population. The mean SFC peak location was measured from the average SFC across all animals. The PSR peak location was measured individually for each recording site then

averaged across the population. Error bars show the standard error of the mean. **(D)** Population mean of the bandwidth of driven activity measured in by the width of the PSR for each pulse duration across all subjects. Error bars show the standard error of the mean.

Figure 5. Site specific E-I windows generate different dynamics. (A) Transduction patterns and network connectivity can vary within a single injection site or across injection sites or subjects. **(B)** At the example site from Fig 3 (Site A) a 20 ms pulse drives a longer evoked response in the LFP (dotted gray). This can be modelled as an E-I window (black) with excitatory (blue) and inhibitory (red) components that have extended durations. This empirical E-I window generates coherent dynamics at low frequencies with a more narrow bandwidth. The E-I window parameters are A=0.097, α_{exc}=2, α_{inh}=4, β_{exc}=4.548, β_{inh}=4.730. **(C)** Same as (B) for Site A, with a 5 ms wide pulse. The E-I window parameters are A=0.097, α_{exc} =1, α_{inh} =3, β_{exc} =2.568, β_{inh} =3.654. **(D)** Same as (C) for a different site. The E-I window parameters are A=0.075, α_{exc} =1, α_{inh} =2, β_{exc} =4.312, β_{inh} =3.445.

Figure 6. E-I window model for mapping parameterization. (A) Example E-I window for empirical data using a 10 ms pulse duration temporally scaled to simulate E-I windows for 5 ms (blue), 20 ms (green), and 50 ms (purple) pulses. **(B)** Right, Simulated PSRs for 2-50ms pulses using an example excitation window from the 10 ms condition. Black dots show the actual PSR peak location from the experimental data. Right, PSRs for simulated responses for 5 ms, 10 ms, 20 ms, and 50 ms pulse widths conditions. Lighter, thinner lines show PSRs for experimental data. **(C)** Same as B for simulated SFC. **(D)** E-I window model parameter for all pulse widths in (B,C).

Figure 7. E-I window model predictions for quasi-periodic stimulation. (A) Quasi-periodic stimulation to generate stimulation pulses according to probability $P(stim) = \beta(1+\alpha\sin(2\pi Ft))\Delta t$.

β is the baseline stimulation rate and α is the modulation depth of stimulation. F is the frequency of interest. Δt is the sampling rate of the simulation pulse train. Increasing α increases stimulation intensity at frequency F. **(B)** Simulated PSR for fully periodic stimulation (F = 35 Hz) with 15 ms evoked potentials. Inset, Linear model prediction. **(C)** Simulated PSR for quasi-periodic stimulation (F = 35 pulse/s, α = 20, β = 5). **(D)** Trial-by-trial PSRs for the simulated responses from C. **(E)** Simulated PSR when varying modulation depth α. Other parameters as in C. **(F)** Simulated SFC when varying modulation depth α (F = 25 Hz). **(G)** Simulated PSR when varying frequency F. Other parameters as in C. **(H)** Simulated PSR using evoked potentials from 2 ms pulses for F = 65 Hz (red) compared with results from C (blue).

Figure 1

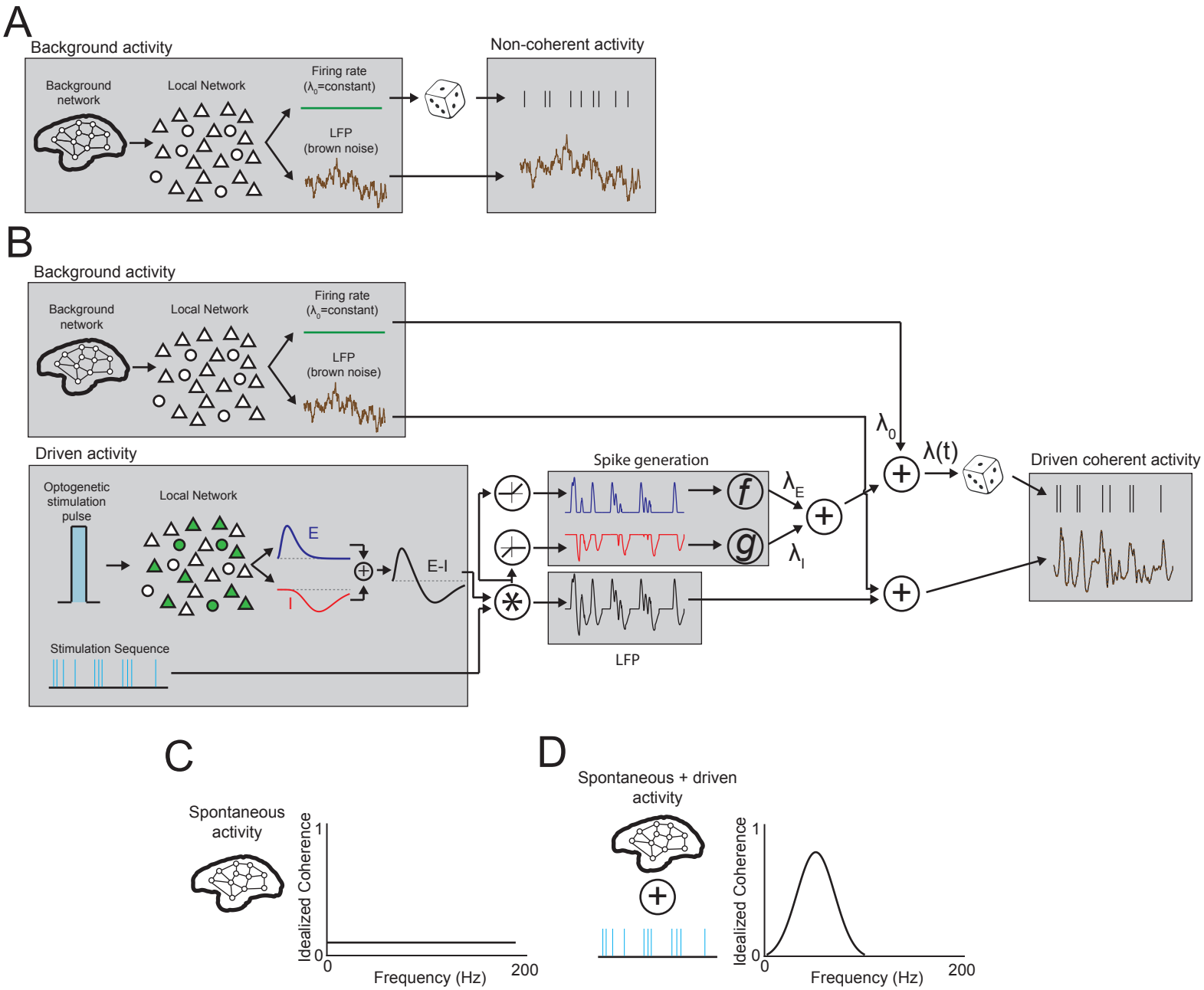

Figure 1. Excitation and inhibition drive coherent neuronal dynamics. (A) During spontaneous activity, synaptic inputs drive activity in a local network. We model spiking as being generated from a Poisson process with a constant rate and LFP as being generated from a Brown noise process. Under these assumptions, spontaneous spiking is not coherent with spontaneous LFP. **(B)** To model of optogenetic stimulation of a population of transduced neurons, we simulated pulsatile responses generated by direct activation of ChR2 channels and synaptic activity. Pulsatile responses are convolved with a stimulation sequence. The summed excitatory and inhibitory (E-I, black) components comprise the simulated LFP. The individual E (blue) and I (red) activity govern the variable spiking rate in the Poisson process which generates coherent spiking. **(C)** Spontaneous activity in the model has no spike-field coherence. **(D)** Optogenetic stimulation drives correlated fields and spiking, leading to frequency selective spike-field coherence.

Figure 2

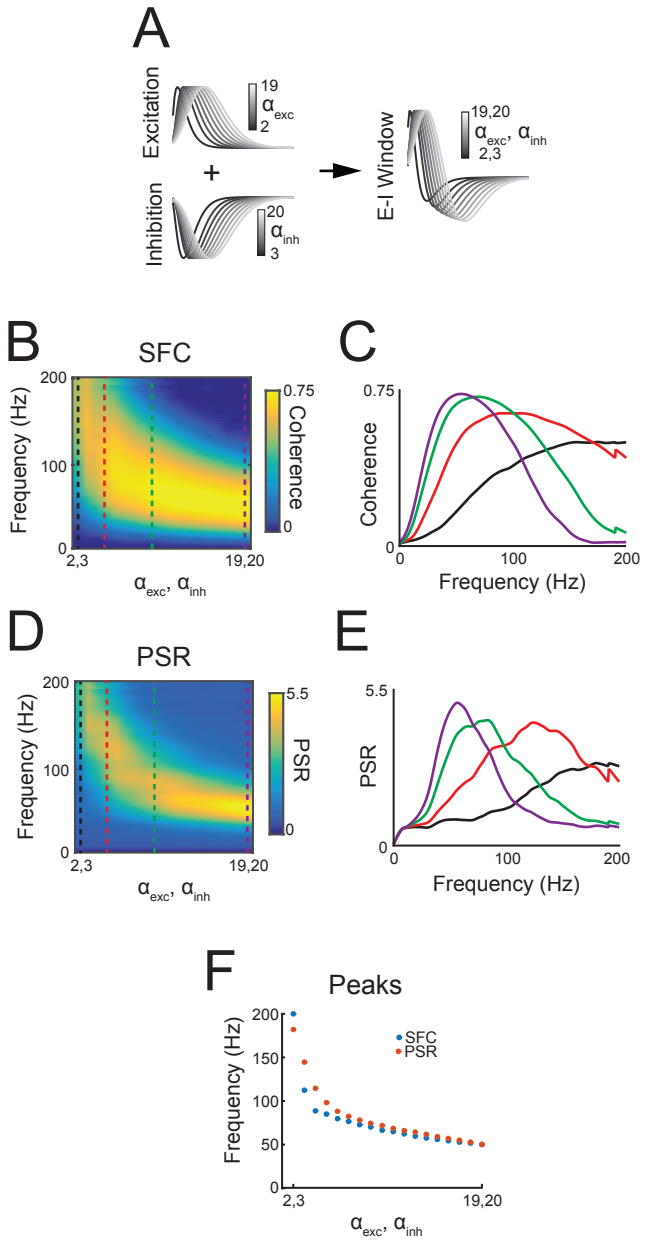

Figure 2. E-I window shape controls frequency of coherent activity. (A) Excitation, inhibition and E-I windows generated when varying α_{exc} and setting $\alpha_{inh} = \alpha_{exc} + 1$ to alter the duration of the windows. E-I is the sum of E and I windows. **(B)** Spike-field coherence that results from using the E-I windows from (A) in the model. E-I duration is measured as the time from the onset of the response and when the response returns to the stable state. **(C)** Example coherence for various E-I windows in (B). **(D)** Power spectral ratio that results from using the E-I windows from (A) in the model. **(E)** Example PSRs for various E-I windows in (D). **(F)** Right, frequency of peaks in the SFC (blue) and PSR (red) for each E-I window in (A).

Figure 3

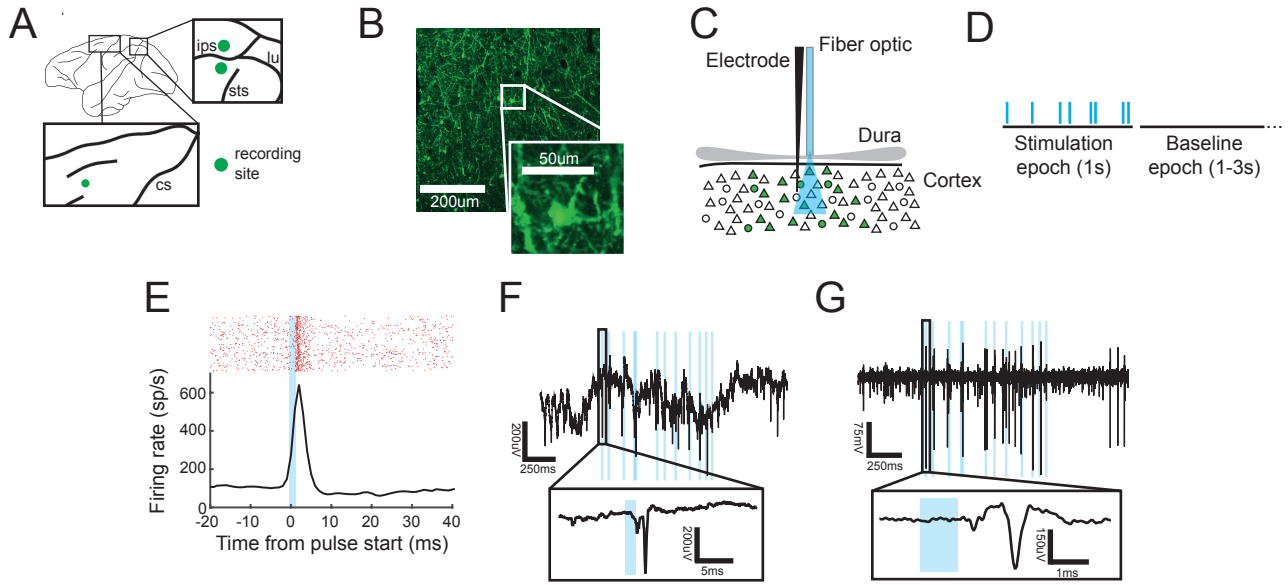

Figure 3. Optogenetic stimulation in macaque cortex. (A) Recording locations in all animals. The area of the circle corresponds to the number of sites recorded in each animal. **(B)** Example injection site with YFP labeled neurons and neuropil from horizontal section. Inset: image of a single transduced neuron. **(C)** Recordings were performed with a single, acute electrode during trans-dural light stimulation with a fiber optic place over a surgically thinned dura. **(D)** Experimental design featured a 1 s stimulation pulse sequence followed by 1-3 s without stimulation. **(E)** Example raster plot (top) and PSTH (bottom) of the spiking response triggered on each stimulation pulse for Poisson distributed trains of 1 ms pulses at 10 pulse/s rate. **(F)** Example broadband recording during a pulse train containing 1 ms pulses at 10 pulse/s rate; optogenetic stimulation (blue). Inset: Response to a single pulse. **(G)** Example multiunit filtered data from (E). Inset: Stimulation-elicited spike.

Figure 4

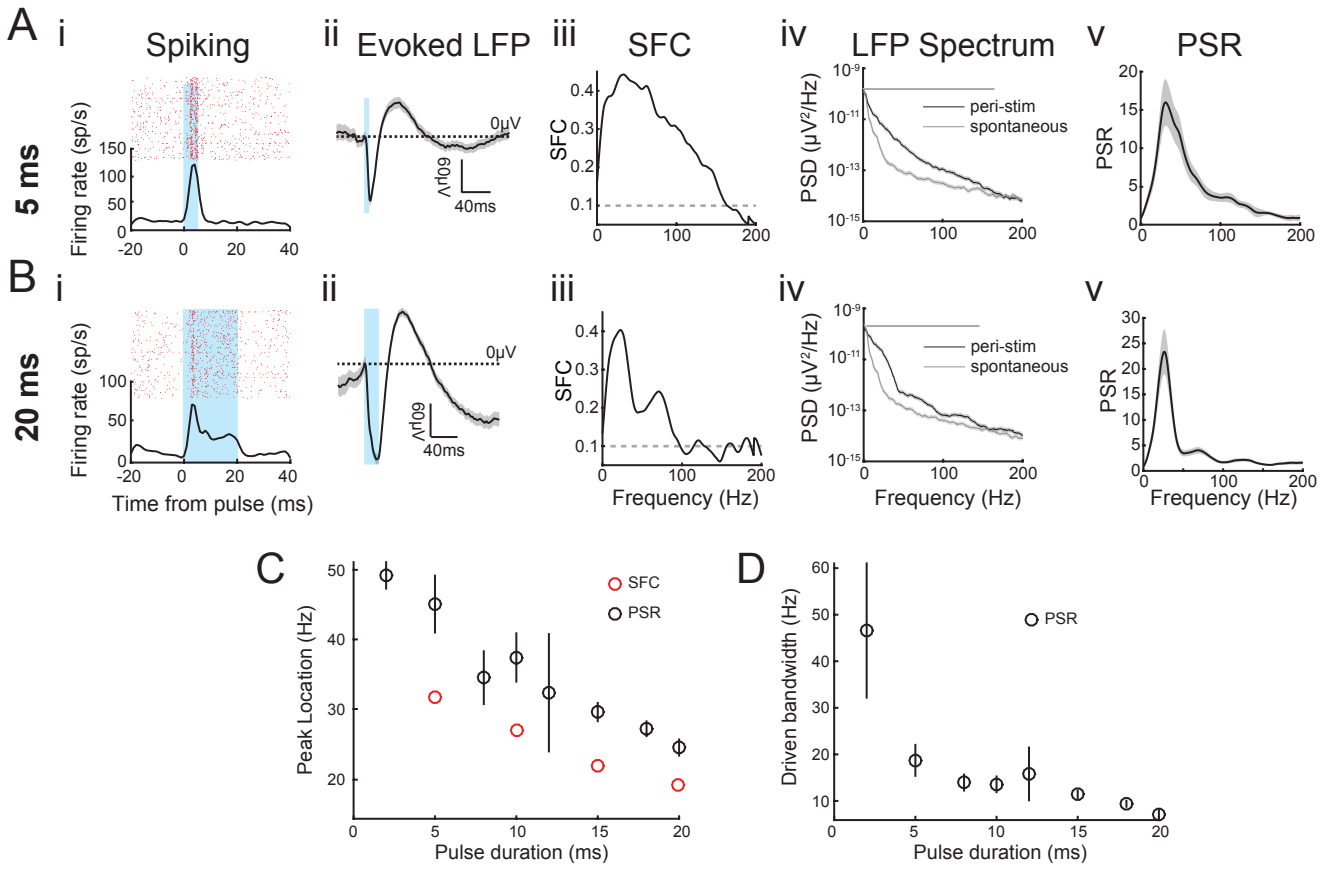

Figure 4. Neuronal dynamics driven by optogenetic stimulation. (A) Neuronal responses to 5 ms pulse duration, 20 Hz pulse rate, periodic pulse train. (i) Raster (top) and PSTH (bottom) of the response to single light pulses (blue). (ii) Mean evoked potential for all the stimulation pulses that were the last in a sequence and not preceded by a prior stimulation pulse within 50 ms, normalized by subtracting the value of the LFP at the onset of the light. Dotted line indicates 0 mV. (iii) Spike-field coherence for multi-unit activity and LFP measured on the same electrode. Dotted horizontal line shows expected coherence under the null hypothesis that coherence is zero. (iv) Power spectral density (PSD) of 1 s of data during stimulation (black line) and spontaneous activity prior to stimulation (grey line). The dotted lines are error bars determined by the Chi-squared test for p=0.01. Solid gray lines above the PSD illustrate frequency bands where the stimulus PSD was significantly different from the spontaneous PSD (p<0.01). (v) Power spectral ratio showing frequency specific increases in power due to stimulation. **(B)** Same as (A) for 20 ms, 20 pulses/s pulse rate, Poisson pulse train. **(C)** Population mean of peak frequency for the SFC (red) and PSR (black) for each pulse duration across all subjects. The mean SFC peak location was measured from the average SFC across the population. The PSR peak location was measured individually for each recording site then averaged across the population. Error bars show the standard error of the mean. **(D)** Population mean of the bandwidth of driven activity measured in by the width of the PSR for each pulse duration across all subjects. Error bars show the standard error of the mean.

Figure 5

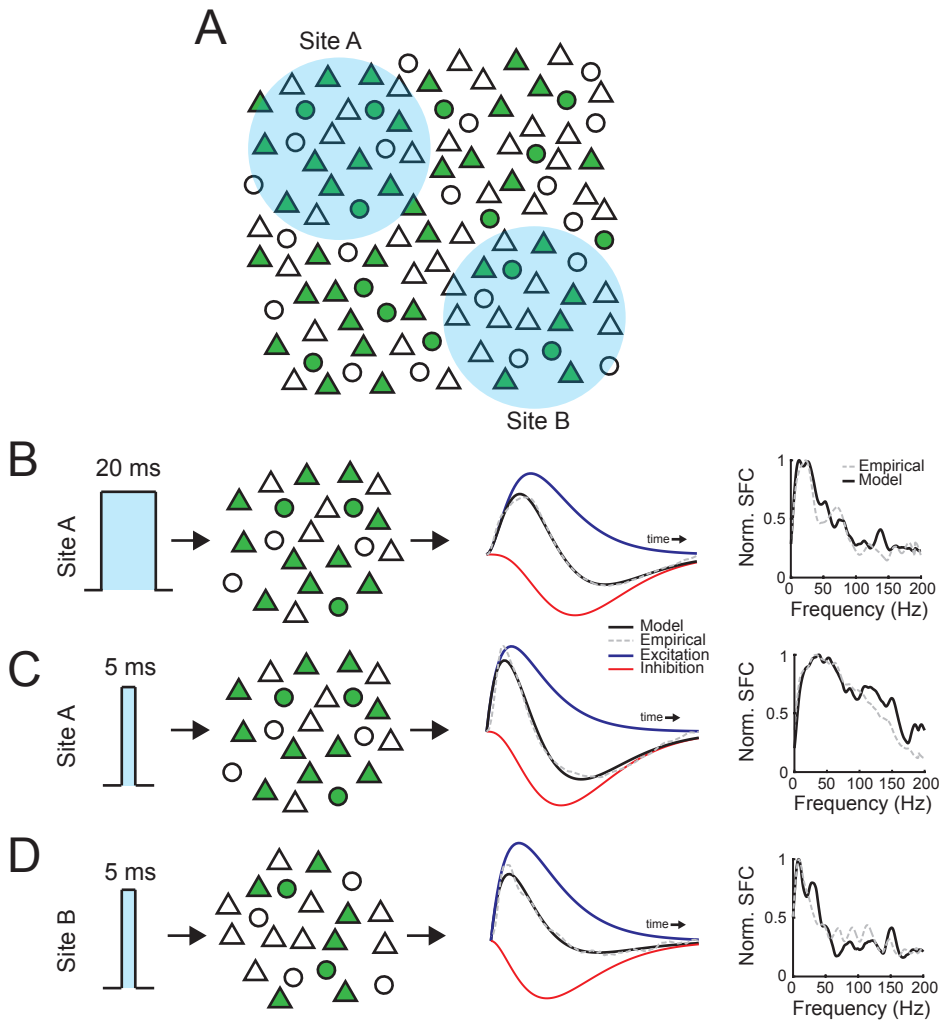

Figure 5. Site specific E-I windows generate different dynamics. (A) Transduction patterns and network connectivity can vary within a single injection site or across injection sites or subjects. **(B)** At the example site from Fig 3 (Site A) a 20 ms pulse drives a longer evoked response in the LFP (dotted gray). This can be modelled as an E-I window (black) with excitatory (blue) and inhibitory (red) components that have extended durations. This empirical E-I window generates coherent dynamics at low frequencies with a more narrow bandwidth. The E-I window parameters are A=0.097, α_{exc}=2, α_{inh}=4, β_{exc}=4.548, β_{inh}=4.730. **(C)** Same as (B) for Site A, with a 5 ms wide pulse. The E-I window parameters are A=0.097, α_{exc}=1, α_{inh}=3, β_{exc}=2.568, β_{inh}=3.654. **(D)** Same as (C) for a different site. The E-I window parameters are A=0.075, α_{exc}=1, α_{inh}=2, β_{exc}=4.312, β_{inh}=3.445.

Figure 6

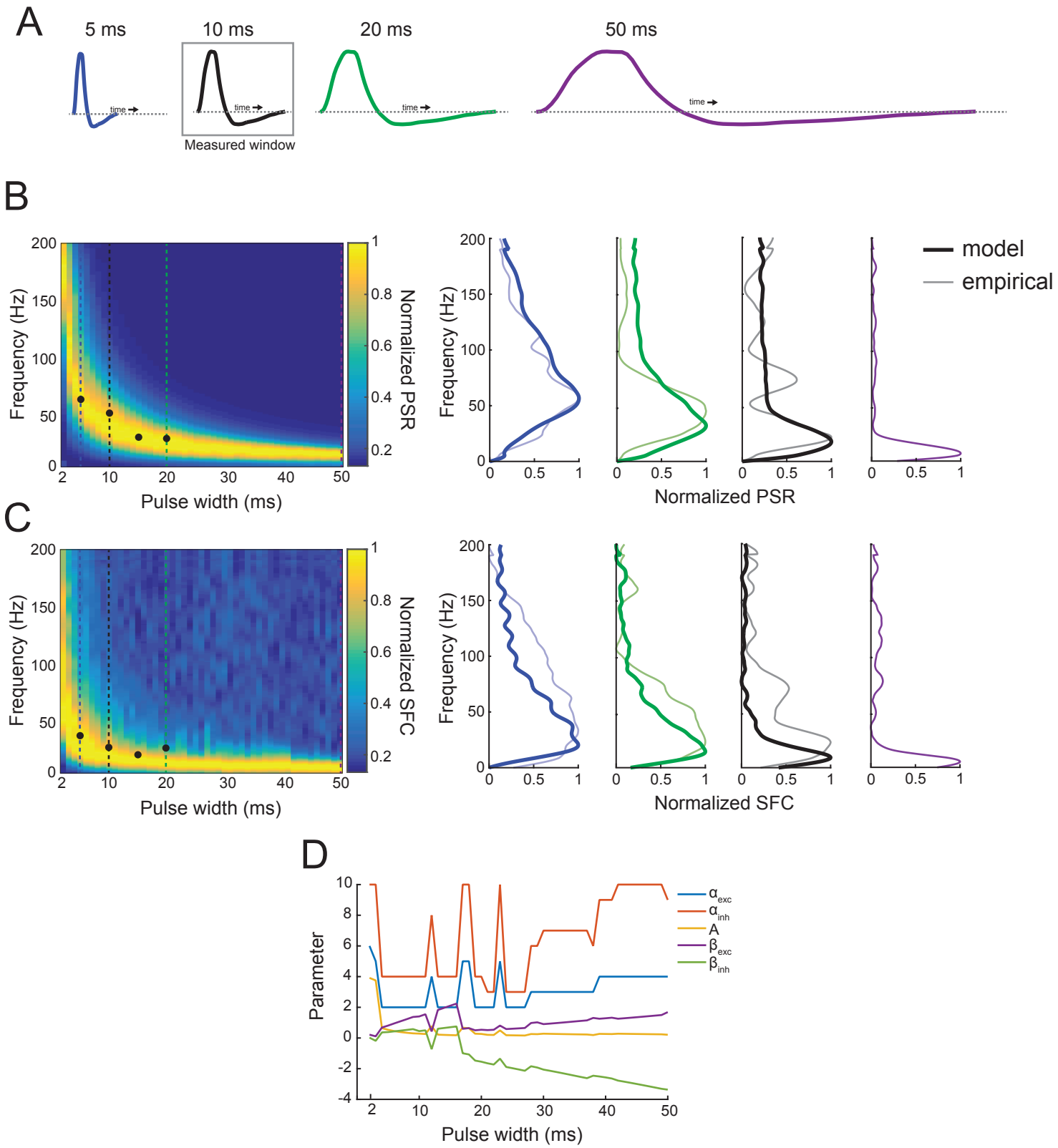

Figure 6. E-I window model for mapping parameterization. (A) Example E-I window for empirical data using a 10 ms pulse duration temporally scaled to simulate E-I windows for 5 ms (blue), 20 ms (green), and 50 ms (purple) pulses. **(B)** Right, Simulated PSRs for 2-50ms pulses using an example excitation window from the 10 ms condition. Black dots show the actual PSR peak location from the experimental data. Right, PSRs for simulated responses for 5 ms, 10 ms, 20 ms, and 50 ms pulse widths conditions. Lighter, thinner lines show PSRs for experimental data. **(C)** Same as B for simulated SFC. **(D)** E-I window model parameter for all pulse widths in (B,C).

Figure 7

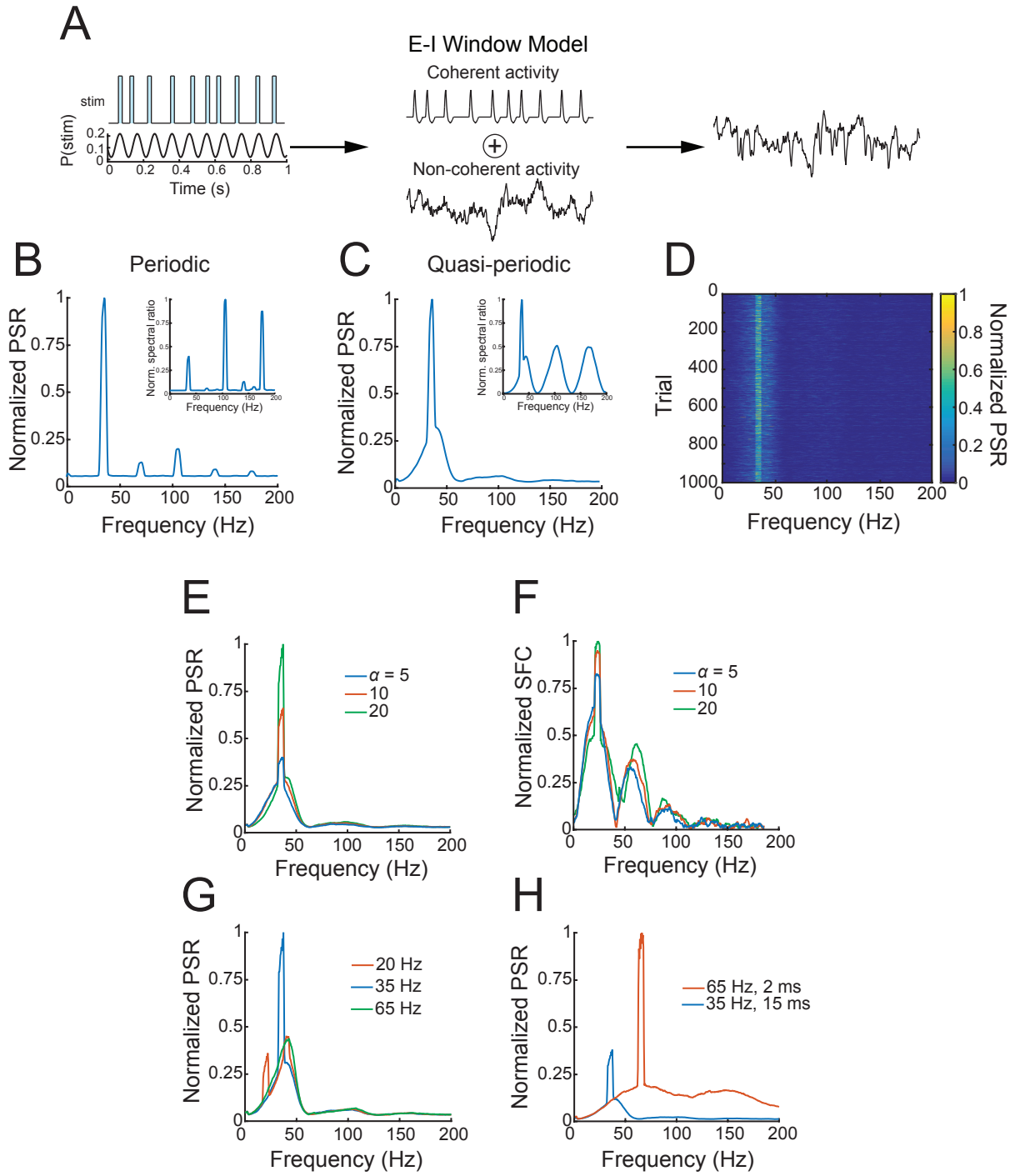

Figure 7. E-I window model predictions for quasi-periodic stimulation. (A) Quasi-periodic stimulation to generate stimulation pulses according to probability P(stim) = β(1+αsin(2πFt))Δt. β is the baseline stimulation rate and α is the modulation depth of stimulation. F is the frequency of interest. Δt is the sampling rate of the simulation pulse train. Increasing α increases stimulation intensity at frequency F. **(B)** Simulated PSR for fully periodic stimulation (F = 35 Hz) with 15 ms evoked potentials. Inset, Linear model prediction. **(C)** Simulated PSR for quasi-periodic stimulation (F = 35 pulse/s, α = 20, β = 5). **(D)** Trial-by-trial PSRs for the simulated responses from C. **(E)** Simulated PSR when varying modulation depth α. Other parameters as in C. **(F)** Simulated SFC when varying modulation depth α (F = 25 Hz). **(G)** Simulated PSR when varying frequency F. Other parameters as in C. **(H)** Simulated PSR using evoked potentials from 2 ms pulses for F = 65 Hz (red) compared with results from C (blue).